

Article

Time Evolution Characterization of Atmospheric-Pressure Plasma Jet (APPJ)-Synthesized Pt-SnO_x Catalysts

Chia-Chun Lee ¹, Tzu-Ming Huang ^{1,2}, I-Chun Cheng ^{3,4,*} , Cheng-Che Hsu ^{5,*} and Jian-Zhang Chen ^{1,2,*} 

¹ Graduate Institute of Applied Mechanics, National Taiwan University, Taipei 10617, Taiwan; r05543015@ntu.edu.tw (C.-C.L.); r06543009@ntu.edu.tw (T.-M.H.)

² Advanced Research Center for Green Materials Science and Technology, National Taiwan University, Taipei 10617, Taiwan

³ Graduate Institute of Photonics and Optoelectronics, National Taiwan University, Taipei 10617, Taiwan

⁴ Department of Electrical Engineering, National Taiwan University, Taipei 10617, Taiwan

⁵ Department of Chemical Engineering, National Taiwan University, Taipei 10617, Taiwan

* Correspondence: iccheng@ntu.edu.tw (I.-C.C.); chsu@ntu.edu.tw (C.-C.H.); jchen@ntu.edu.tw (J.-Z.C.); Tel.: +886-2-33669648 (I.-C.C.); +886-2-33663034 (C.-C.H.); +886-2-33665694 (J.-Z.C.)

Received: 17 August 2018; Accepted: 29 August 2018; Published: 1 September 2018



Abstract: We characterize the time evolution (≤ 120 s) of atmospheric-pressure plasma jet (APPJ)-synthesized Pt-SnO_x catalysts. A mixture precursor solution consisting of chloroplatinic acid and tin(II) chloride is spin-coated on fluorine-doped tin oxide (FTO) glass substrates, following which APPJ is used for converting the spin-coated precursors. X-ray photoelectron spectroscopy (XPS) indicates the conversion of a large portion of metallic Pt and a small portion of metallic Sn (most Sn is in oxidation states) from the precursors with 120 s APPJ processing. The dye-sensitized solar cell (DSSC) efficiency with APPJ-synthesized Pt-SnO_x CEs is improved greatly with only 5 s of APPJ processing. Electrochemical impedance spectroscopy (EIS) and Tafel experiments confirm the catalytic activities of Pt-SnO_x catalysts. The DSSC performance can be improved with a short APPJ processing time, suggesting that a DC-pulse nitrogen APPJ can be an efficient tool for rapidly synthesizing catalytic Pt-SnO_x counter electrodes (CEs) for DSSCs.

Keywords: atmospheric pressure plasma jet; platinum; tin oxide; dye-sensitized solar cells; chloroplatinic acid; tin chloride

1. Introduction

Atmospheric-pressure plasma (APP) technology is operated without using a vacuum chamber and associated pumping system. It is therefore considered a cost-effective manufacturing tool. Recent developments have resolved stability and arcing problems, making APP technology promising for industrial applications. Traditional APP sources include transferred arc, corona discharge, dielectric barrier discharge, and atmospheric pressure plasma jet (APPJs) [1,2]. APPs with various heavy particle temperatures and charge densities can be produced by using different excitation methods and electrode configuration designs. The synergy between the reactive plasma species and heat can promote rapid chemical reactions during material processing [3–6]. APPs have been used for processing various types of materials, such as carbon nanotubes [3,7,8] and reduced graphene oxides [9–11]. Applications of APPs for surface cleaning or modification [12–14], deposition of metal oxides [15,16], and syntheses of metal compounds from liquid precursors [6,17,18] have been extensively investigated.

Metals and metal oxides are common catalysts [19–24]. APPs also have been used for syntheses and post-treatments of catalysts [25].

In 1991, Grätzel et al. reported a great breakthrough of DSSCs [26], and since then, dye-sensitized solar cells (DSSCs) have been extensively investigated. A conventional DSSC consists of a dye-adsorbed photoanode, an electrolyte, and a counter electrode (CE). A catalytic CE is used for reducing triiodide into iodine in the electrolyte. Generally, Pt is the most commonly used CE material in DSSC, owing to its high catalytic activity and stability [27]. Various alternative CE materials such as carbon-based materials, metal oxides or chalcogenides, and alloys or intermetallics have been studied extensively [3,5,28–36]. Composites containing Pt and Sn have been used as electrocatalysts for CEs of DSSCs [36,37], methanol or ethanol oxidation [38–44], aqueous phase oxidation [45], and gas sensing [46]. The addition of metal oxides has been reported to improve the catalytic activity [40,47]. Pt:SnO₂ electrocatalytic films were used as CEs of DSSCs [48]. Dao et al. fabricated DSSCs with a PtSn alloy supported by reduced graphene oxides via dry plasma reduction [36]. In the present study, Pt-SnO_x composites were synthesized by mixing chloroplatinic acid and tin(II) chloride that were processed using a DC-pulse nitrogen APPJ. X-ray photoelectron spectroscopy (XPS) results showed that the majority of Sn was in the oxidation state. The DSSC efficiency can be improved rapidly through 5 s APPJ processing of the chloroplatinic acid and tin(II) chloride mixture precursor; no metallic Pt was converted within such a short processing time. This suggests the catalytic effect of oxidized Pt and Sn compounds. A DSSC with a 120 s APPJ-processed Pt-SnO_x CE shows efficiency comparable to that of a cell with a furnace-processed Pt CE.

2. Materials and Methods

2.1. Preparation of Pt-SnO_x CEs

25-mM chloroplatinic acid (H₂PtCl₆) (purity: 99.95%, Uniregion Biotech, Taipei, Taiwan) and 25-mM tin(II) chloride (SnCl₂) isopropanol solutions were separately stirred for 24 h. These two solutions were mixed with the same volume ratios and were stirred using a magnetic stirrer (PC-420D, Corning Inc., Corning, NY, USA) for another 24 h. Next, 60 μL of the mixture precursor was spin-coated onto fluorine-doped tin oxide (FTO) substrates with an area of 1.5 cm × 1.5 cm at a speed of 1000 rpm for 15 s. The spin-coated precursors were then processed by a nitrogen APPJ for 5, 15, 30, 60, and 120 s. Figure 1a shows the APPJ setup. The operation parameters are as follows: nitrogen flow of 46 standard liter per minute (slm), power supply voltage of 275 V, and ON/OFF duty cycle of 7/33 μs. The temperature evolution of the substrates, shown in Figure 1b, was measured using a K-type thermocouple (OMEGA Engineering, Norwalk, CT, USA). The temperature rapidly increased to ~510 °C, and it dramatically decreased after the APPJ was turned off. Because our process is conducted at ~510 °C, we use FTO glass substrates (Sigma-Aldrich, St. Louis, MO, USA) which can tolerate a higher processing temperature.

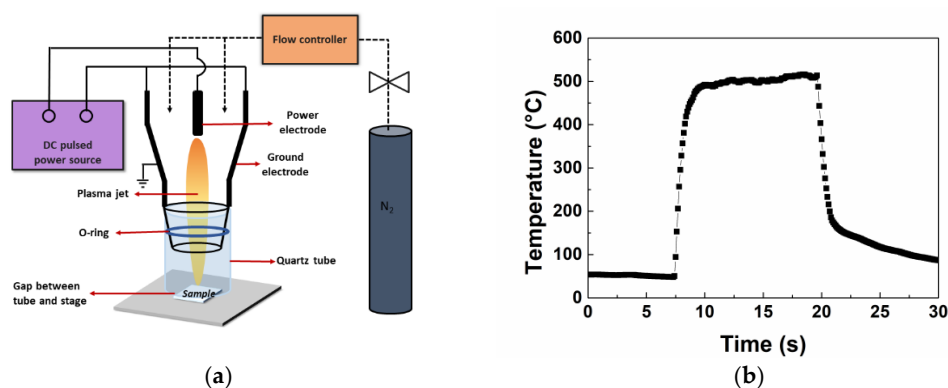


Figure 1. (a) Schematic of APPJ setup; (b) Temperature evolution of substrate during APPJ treatment.

2.2. Preparation of TiO₂ Photoanode and Assembly of DSSCs

The photoanode consists of a TiO₂ compact layer and a TiO₂ nanoporous layer for dye adsorption. First, a 0.23-M titanium isopropoxide solution (Fluka, St. Louis, MO, USA) was spin-coated on a FTO substrate and then baked at 200 °C for 10 min to form a TiO₂ compact layer to prevent electron recombination. Then, 1.6 g of TiO₂ nanoparticles (diameter: ~21 nm), 8 mL of ethanol, 6.49 g of terpineol (anhydrous, #86480, Fluka, St. Louis, MO, USA), 4.5 g of 10 wt % ethyl cellulose ethanolic solution (5–15 mPa·s, #46070, Fluka, St. Louis, MO, USA), and 3.5 g of 10 wt % ethyl cellulose ethanolic solution (30–50 mPa·s, #46080, Fluka, St. Louis, MO, USA) were mixed together. Next, a 0.4 g mixture containing TiO₂ was mixed with 500 µL of ethanol and stirred using a magnetic stirrer for 24 h. The mixed solution was baked at 53 °C until its weight became 0.175 g, thus completing the preparation of the TiO₂ pastes. The TiO₂ pastes were screen-printed onto the TiO₂ compact layer coated FTO substrate with a printed area of 0.5 cm × 0.5 cm. The screen-printed pastes were calcined at 510 °C for 15 min in a conventional furnace to form the TiO₂ photoanode. Next, the TiO₂ photoanode was immersed in a 0.3-mM N719 solution, which is mixed with acetonitrile and tertbutyl alcohol in a 1:1 volume ratio for 24 h. This completed the preparation of the dye-anchored nanoporous TiO₂ photoanodes.

The Pt-SnO_x CEs and dye-anchored TiO₂ photoanodes were assembled with a 25-µm-thick spacer to form sandwich-structure DSSCs. Then, a commercial electrolyte (E-Solar EL 200, Everlight Chemical Industrial Co., Taipei, Taiwan) was injected into the solar cells.

Counterpart DSSC with furnace-processed Pt CE was fabricated for comparison. In this case, 60 µL of 25-mM H₂PtCl₆ isopropanol solution was spin-coated on the FTO substrate and calcined at 400 °C for 15 min using a tube furnace. The assembly procedure of DSSC with furnace-processed Pt CE is the same as that of DSSC with APPJ-processed Pt-SnO_x CE.

2.3. Characterization of Materials and DSSCs

During the APPJ reduction processes, a spectrometer (USB4000, Ocean Optics, Largo, FL, USA) was used for monitoring the plasma optical emission spectra (OES). Pt-SnO_x nanoparticles were inspected using a scanning electron microscope (SEM, JSM-7800F Prime, JEOL, Tokyo, Japan) with an energy-dispersive spectroscopy (EDS) attachment. To investigate the chemical configuration of Pt-SnO_x, XPS (Thermo K-Alpha, VGS, Waltham, MA, USA) was used for analyzing the binding status. The C1s core level was centered at 284.6 eV to calibrate the binding energy scale. XPSPEAK 4.1 software (was used for fitting binding energy positions. XPS samples were prepared with Corning glass substrates instead of FTO glass ones to avoid the interference of Sn signals emitted from FTO substrates. To examine the electrochemical catalytic activities of Pt-SnO_x CEs, electrochemical impedance spectroscopy (EIS) and Tafel measurements were performed using an electrochemical workstation (PGSTAT204, Metrohm Autolab, Herisau, Switzerland). EIS measurements were performed with a sinusoidal amplitude of 10 mV with frequencies of 0.1-10⁵ Hz, and the data were fitted using Z-view 3.1 software. Tafel curves were recorded from -0.6 V to 0.6 V at a scan rate of 50 mV/s. Both measurements were performed on a symmetrical cell with two equal Pt-SnO_x CEs. A solar simulator (WXS-155S-L2, WACOM, Saitama, Japan) with an AM 1.5 filter equipped with an electrometer (Keithley 2440, Tektronix, Beaverton, OR, USA) was used for measuring the photocurrent-voltage characteristics of the DSSCs.

3. Results and Discussion

Figure 2a shows the plasma OES evolution during APPJ processing of the mixed H₂PtCl₆/SnCl₂ precursor. NO_γ, NO_β, N₂ 1st positive, and N₂ 2nd positive emissions were observed clearly during 120 s APPJ processes. Figure 2b shows the plasma spectra when processing H₂PtCl₆, SnCl₂, and mixed H₂PtCl₆/SnCl₂ precursors on the FTO substrates. The NO_γ system (A²Σ⁺-X²Π) is located at wavelengths lower than 280 nm. The NO_β system (B²Π-X²Π) is located from around 260 to 500

nm, and it partially overlaps the NO_γ system. The other emissions at 357, 385, and 389 nm were attributed to the N_2 2nd positive system ($\text{C}^3\Pi_u\text{-B}^3\Pi_g$); these overlap with the NO_β system. The N_2 1st positive system ($\text{B}^3\Pi_g\text{-A}^3\Sigma_u^+$) was located at wavelengths higher than 530 nm.

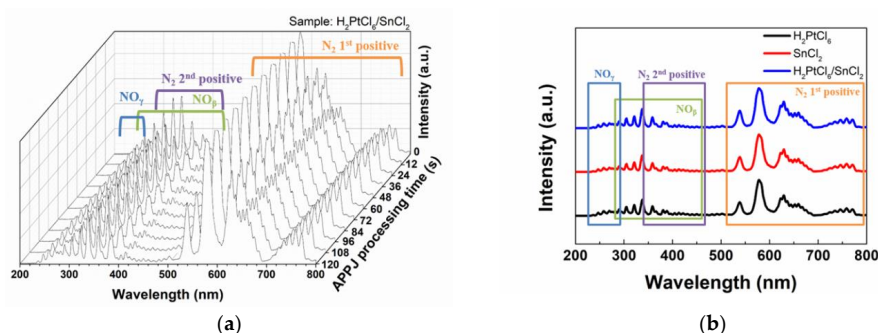


Figure 2. (a) OES evolution during APPJ processing of mixed $\text{H}_2\text{PtCl}_6/\text{SnCl}_2$ precursors. (b) OES when processing H_2PtCl_6 , SnCl_2 , and mixed $\text{H}_2\text{PtCl}_6/\text{SnCl}_2$ precursors using nitrogen APPJ.

Figure 3a–e shows the SEM images of Pt-SnO_x nanoparticles converted from mixed $\text{H}_2\text{PtCl}_6/\text{SnCl}_2$ precursors on the FTO glass substrates using various APPJ processing times. The nanoparticle size and morphology remained similar for APPJ processing times of 5–120 s. Figure 3f shows EDS results for the 120 s and APPJ-processed sample. Pt and Sn signals indicate the presence of two elements in the nanoparticles. Both of Sn and O signals could result from the nanoparticles and the FTO substrates.

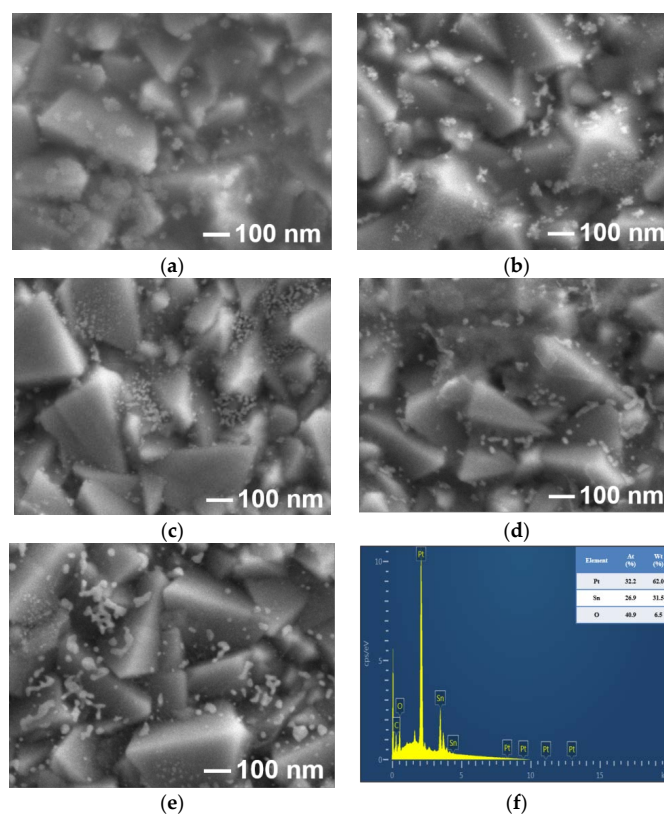


Figure 3. Scanning electron microscope (SEM) images of samples processed by APPJ for various durations: (a) 5 s, (b) 15 s, (c) 30 s, (d) 60 s, and (e) 120 s. (f) Energy-dispersive spectroscopy (EDS) spectrum of nanoparticles converted from $\text{H}_2\text{PtCl}_6/\text{SnCl}_2$ precursors on FTO glass substrates using 120 s APPJ processing.

To identify the chemical states of Pt-SnO_x compounds, Figure 4a,b shows the XPS spectra of Pt4f and Sn3d for samples. The Pt4f spectrum can be deconvoluted into three components including Pt, Pt²⁺, and Pt⁴⁺. The metallic peaks of Pt are located at 71.30 and 74.65 eV, Pt(II) components are located at 72.70 and 76.50 eV, and Pt(IV) components are located at 73.80 and 77.15 eV [49,50]. In Figure 4a, the major peaks belong to Pt²⁺ and Pt⁴⁺ for as-deposited and 5 and 15 s APPJ-processed samples. These results indicate that most of the H₂PtCl₆/SnCl₂ precursor was not converted to metallic Pt by APPJ processing for less than 15 s. As the APPJ processing time increases, increased conversion of precursors into metallic Pt was clearly observed. The Pt²⁺ signal is noted as the oxidation state of Pt, and it could indicate PtO [51,52] or Pt(OH)₂ [53]. The presence of Pt oxidation states, due to the interaction with the Pt-support, is attributed to an electronic effect or oxygen absorption from air [54,55]. Figure 4b shows the oxidation state of Sn3d under various APPJ processing times. The binding energy of Sn3d can be deconvoluted into two categories: one at 485.8 and 494.2 eV for the zero-valent state of Sn, and the other at 487.3 and 495.7 eV for Sn(II/IV) components [56]. The major peak is attributed to the oxidation state of Sn for up to 120 s, and the percentage of metallic Sn increased only slightly with the APPJ processing time. Sn(II) and Sn(IV) species are difficult to distinguish from XPS measurements because of the small difference between their binding energies [57,58]. Tables 1 and 2 show the percentages of Pt and Sn species, respectively. The Pt-support interaction may influence charge transfer from Pt to oxygen species on the surface and improve the electrochemical catalytic abilities and catalyst stability [47].

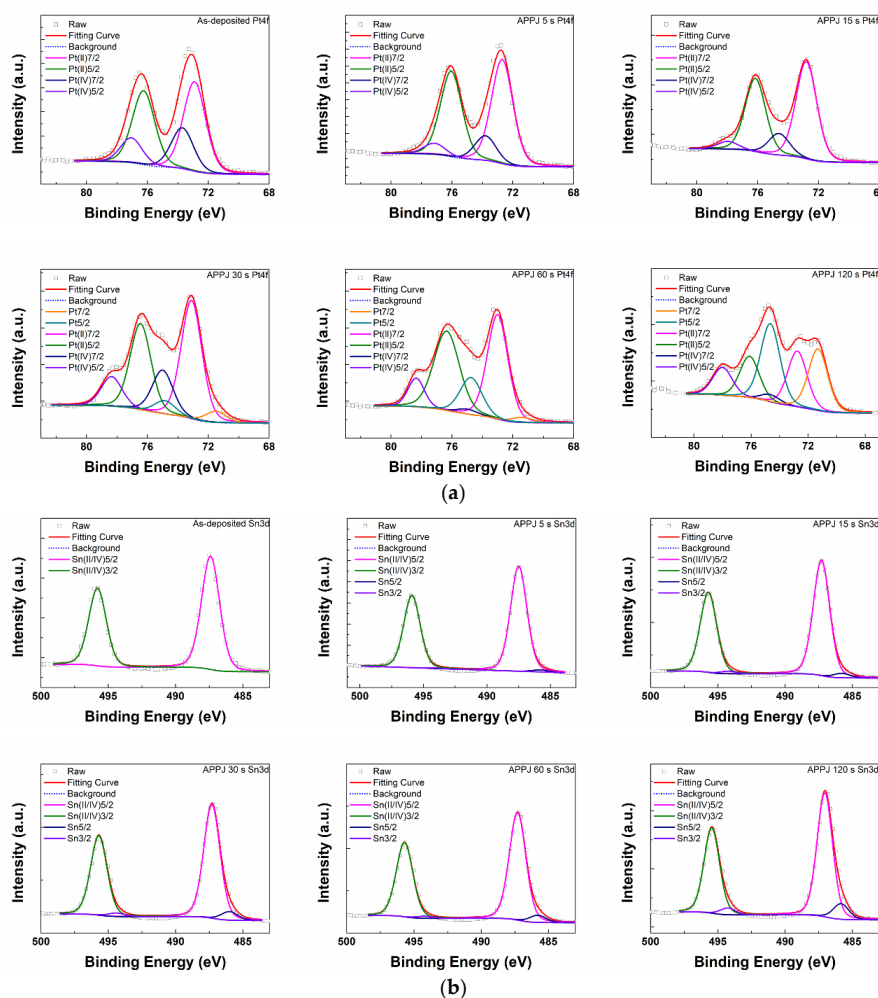


Figure 4. X-ray photoelectron spectroscopy (XPS) spectra of (a) Pt4f and (b) Sn3d for samples processed by APPJ for various durations.

Table 1. Percentage of Pt species obtained from XPS analysis.

APPJ Pt4f (%)	Pt 7/2	Pt 5/2	Pt(II) 7/2	Pt(II) 5/2	Pt(IV) 7/2	Pt(IV) 5/2
0 s	-	-	39.19	32.34	17.90	10.58
5 s	-	-	46.17	37.94	10.90	4.99
15 s	-	-	48.87	36.29	10.87	3.97
30 s	3.72	4.38	39.16	28.52	14.39	9.82
60 s	1.87	14.34	38.04	35.64	1.80	8.31
120 s	22.66	28.72	20.46	15.21	2.69	10.26

Table 2. Percentage of Sn species obtained from XPS analysis.

APPJ Sn3d (%)	Sn 5/2	Sn 3/2	Sn(II/IV) 5/2	Sn(II/IV) 3/2
0 s	-	-	60.19	39.81
5 s	1.13	0.36	58.33	40.19
15 s	2.21	1.31	56.95	39.53
30 s	4.17	1.72	55.35	38.76
60 s	3.72	1.14	56.27	38.87
120 s	6.72	2.93	53.51	36.84

Figure 5a,b shows the EIS Nyquist and Bode phase plots to evaluate the catalytic activities of APPJ-processed Pt-SnO_x CEs. The inset of Figure 5a shows the equivalent circuit for Nyquist curve fitting [59]. The series resistance (R_s) and charge-transfer resistance (R_{ct}) can be described as the resistance of substrates and the catalytic effect of the electrode-reducing triiodide ions, respectively. R_s can be obtained from the high-frequency intercept on the real axis and R_{ct} , from the radius of the real semi-circle [60]. Table 3 shows the EIS parameters including R_s , R_{ct} , and constant phase element (CPE1) [29]. A higher catalytic effect and lower charge-transfer resistance would improve the DSSC performance. For all cases, R_s of Pt-SnO_x CEs remained similar. R_{ct} generally decreased (i.e., semi-circle became smaller) as the APPJ processing time increased, indicating that APPJ processing can enhance the catalytic activity. R_{ct} was comparable for APPJ processing times of 60 s (4.72 Ω) and 120 s (4.69 Ω). Lower R_{ct} results in a higher electrocatalytic activity at the interface between the CEs and the electrolytes [61]. CPE1, which represents the interfacial capacitance between the electrode and the electrolyte, is also a good indicator of the surface activity of CEs [62–64]. The 120 s APPJ-processed CEs had a higher CPE1-T (105.5 $\mu\text{F}/\text{cm}^2$), indicating larger surface reaction between the CE and the electrolyte. Bode phase plots show the electron lifetime for recombination in devices; the electron lifetime is expressed as $\tau_e = 1/(2\pi f_{\text{peak}})$, where f_{peak} is the frequency of the highest peak. Shorter electron lifetime indicates faster charge transfer at the interface between the CE and the electrolyte [64,65]. In Figure 5b, the trend of the electron lifetime follows the EIS results. The 5 s APPJ-processed CE has the smallest peak frequency, indicating the largest electron lifetime with slower charge transfer. Furthermore, electron lifetimes are comparable in 60 s and 120 s APPJ-processed CEs, and this is consistent with the results for R_{ct} .

To further clarify the catalytic activities of Pt-SnO_x CEs, Tafel polarization experiments were conducted and the results are shown in Figure 6. The exchange current density (J_0) was measured by the intercept of the Y-axis (zero voltage) from the tangential line of the curve [66,67]. The 120 s APPJ-processed CEs had a large J_0 , indicating better electrocatalytic activity and lower charge-transfer resistance at the interface of the CE and the electrolyte. Table 3 shows that J_0 increases with the APPJ processing time. APPJ processes enhanced the triiodide reduction reaction [60]. The exchange current density is also proportional to R_{ct} obtained from the EIS measurement. It can be described as $J_0 = RT/nFR_{ct}$, where R is a gas constant; T is temperature; n is the number of electrons involved in the redox reaction; and F is the Faraday's constant [68]. EIS and Tafel measurements both indicate that APPJ-processed Pt-SnO_x electrodes show suitable catalytic performance for use as the CEs of DSSCs.

J_0 increases with the APPJ processing time, indicating that APPJ processing can enhance the catalyst activity of Pt-SnO_x.

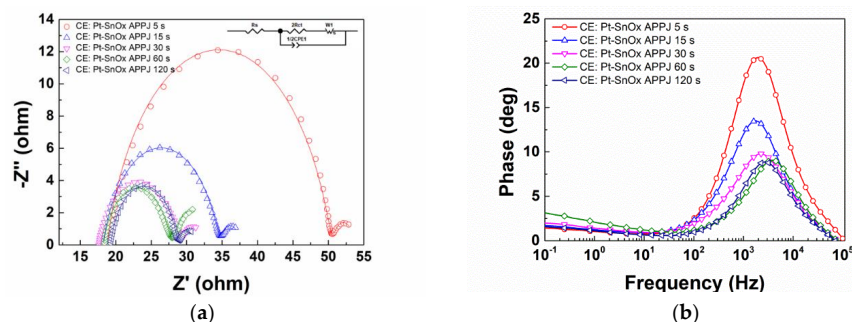


Figure 5. (a) Nyquist curves of symmetric cells with two Pt-SnO_x CEs. The inset shows the equivalent circuit diagram. (b) Bode phase plots of symmetric cells with two Pt-SnO_x CEs.

Table 3. EIS parameters of Pt-SnO_x CEs.

Counter Electrode	R_s (Ω)	R_{ct} (Ω)	CPE1-T ($\mu\text{F}/\text{cm}^2$)	CPE1-P	W1			J_0^a (mA/cm^2)	J_0^b (mA/cm^2)	
					W1-R(Ω)	W1-T(s)	W1-P			
Pt-SnO _x APPJ	5 s	18.8	15.74	35.6	0.835	3.23	2.13	0.5	0.82	1.04
	15 s	18.2	8.18	83.1	0.808	2.82	1.99	0.5	1.58	1.39
	30 s	17.55	5.8	95	0.75	2.73	2.25	0.5	2.23	1.67
	60 s	18.25	4.72	105	0.815	5.04	3.15	0.5	2.74	1.85
	120 s	19.28	4.69	105.5	0.84	2.21	1.8	0.5	2.75	2.08

^a J_0 : Exchange current density is calculated from R_{ct} . ^b J_0 : Exchange current density is calculated from Tafel curve.

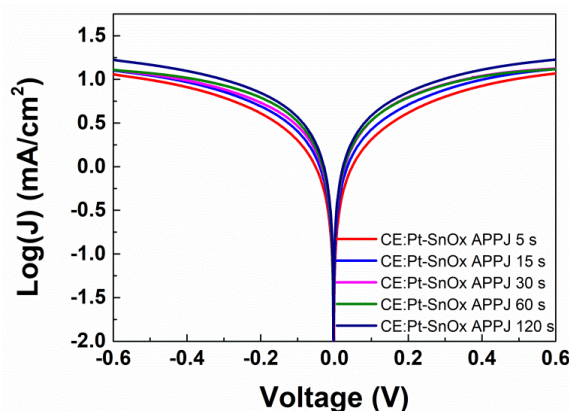


Figure 6. Tafel curves of symmetric cells with various Pt-SnO_x CEs.

Figure 7 shows the IV curves of DSSCs with APPJ-processed Pt-SnO_x CEs. Table 4 shows the photovoltaic parameters, including the open-circuit voltage (V_{oc}), short-circuit current (J_{sc}), fill factor (FF), and efficiency (EFF) with their standard deviations. The power conversion efficiencies (PCEs) of DSSCs with 5 s and 15 s APPJ-processed Pt-SnO_x CEs are $3.87 \pm 0.58\%$ and $3.86 \pm 0.28\%$, respectively, indicating that APPJ processing for a short duration can improve the DSSC performance. XPS results show that almost no metallic Pt was converted with 5 s and 15 s APPJ processing, indicating the catalytic effect of oxidized Pt and Sn compound CEs in DSSCs, and this agrees with previous reported findings [30,32]. As the APPJ treatment time increases, the PCE of DSSCs with 30 s, 60 s, and 120 s APPJ-processed CEs reaches $4.01 \pm 0.34\%$, $4.20 \pm 0.41\%$, and $4.46 \pm 0.29\%$, respectively. The performance of DSSC with a 120 s APPJ-processed Pt-SnO_x CE was comparable to that with a

conventional furnace-processed Pt CE ($4.42 \pm 0.26\%$). Figure 8 shows the statistics of the DSSC parameters. APPJ processing gradually increased the FFs and PCEs of DSSCs, consistent with the results obtained from EIS and Tafel measurement. The improved FF and efficiency with APPJ processing time could result from the better conversion of metallic Pt from the precursor solution.

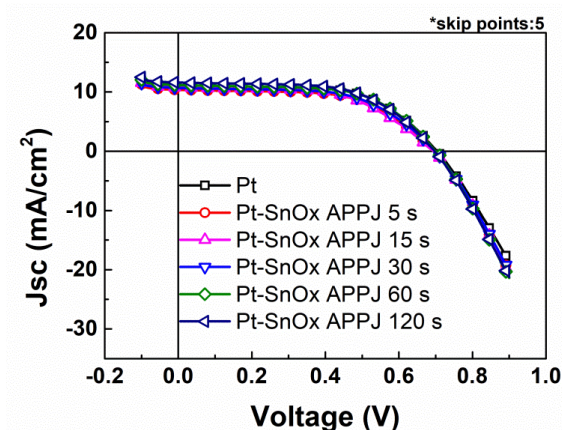


Figure 7. Photocurrent density-voltage curves of DSSCs with various CEs.

Table 4. Photovoltaic parameters of DSSCs with different CEs.

Condition	V_{oc} (V)	J_{sc} (mA/cm ²)	FF (%)	EFF (%)
Pt	0.70 ± 0.02	10.34 ± 0.47	61.27 ± 1.91	4.42 ± 0.26
Pt-SnO _x APPJ				
5 s	0.70 ± 0.01	10.76 ± 0.82	51.65 ± 6.03	3.87 ± 0.58
15 s	0.69 ± 0.02	10.30 ± 0.78	54.43 ± 2.65	3.86 ± 0.28
30 s	0.69 ± 0.02	10.26 ± 0.80	56.38 ± 2.37	4.01 ± 0.34
60 s	0.69 ± 0.02	10.47 ± 0.94	57.91 ± 2.04	4.20 ± 0.41
120 s	0.70 ± 0.02	10.72 ± 0.75	59.41 ± 1.08	4.46 ± 0.29

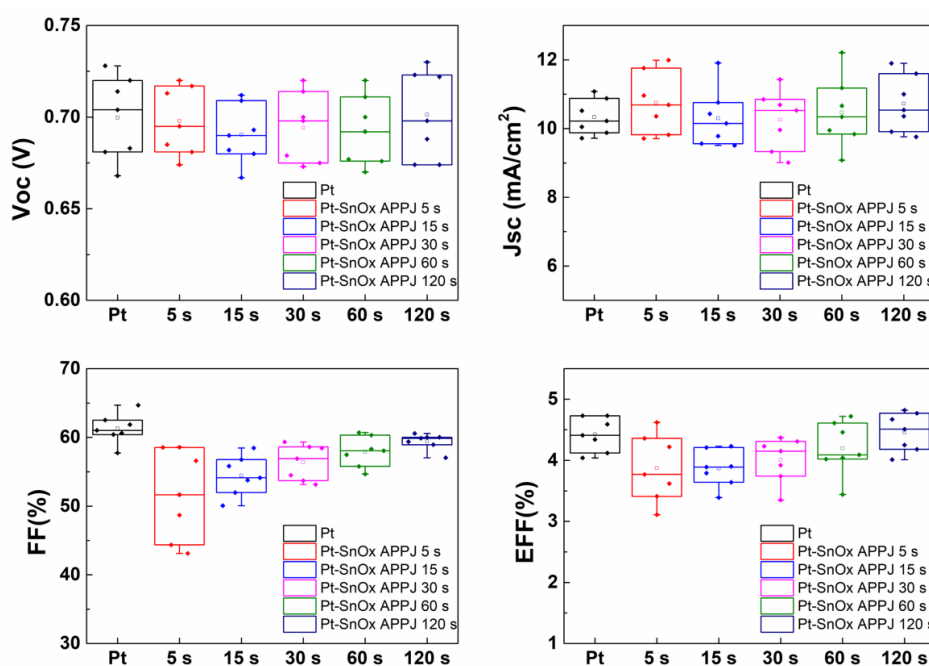


Figure 8. Statistics of DSSC parameters based on APPJ-processed Pt-SnO_x CEs and furnace-processed Pt CE (reference).

4. Conclusions

We analyze the time evolution of Pt-SnO_x nanoparticle catalysts that are converted from a mixture of chloroplatinic acid and tin(II) chloride using DC-pulse nitrogen APPJ. XPS analyses indicate the conversion of a large portion of the metallic Pt and tin oxide. EIS and Tafel measurements indicate improved electrochemical catalytic effects. The synthesized Pt-SnO_x nanoparticles on FTO glass substrates are used as the CEs of DSSCs. The I-V curve shows that the performance of DSSCs with APPJ-processed Pt-SnO_x CEs is comparable to that of DSSCs with conventional furnace-processed Pt CEs. As the APPJ processing time is increased, the FF and efficiency of DSSCs gradually increase. Our results show that a DC-pulse nitrogen APPJ is an efficient tool for synthesizing Pt-SnO_x catalysts from a mixture precursor solution consisting of chloroplatinic acid and tin(II) chloride.

Author Contributions: C.-C.L. performed the experiments, analyzed the data, and wrote the paper draft. T.-M.H. assisted in conducting experiments. I.-C.C. and C.-C.H. assisted in instructing the research and analyzing the data. J.-Z.C. directed the research direction, analyzed the data, and revised the paper. All authors commented on the manuscript.

Funding: This work is supported by the “Advanced Research Center for Green Materials Science and Technology” from The Featured Area Research Center Program of the Higher Education Sprout Project by the Ministry of Education (107L9006) and the Ministry of Science and Technology in Taiwan (MOST 105-2221-E-002-047-MY3, MOST 106-2221-E-002-193-MY2 & MOST 107-3017-F-002-001).

Acknowledgments: The cleanroom facility is provided by the Nano-Electro-Mechanical-Systems (NEMS) Research Center at National Taiwan University. Yuan-Tzu Lee of the Instrumentation Center at National Taiwan University helps with the SEM operation.

Conflicts of Interest: The authors declare no conflict of interest.

References

1. Schutze, A.; Jeong, J.Y.; Babayan, S.E.; Park, J.; Selwyn, G.S.; Hicks, R.F. The atmospheric-pressure plasma jet: A review and comparison to other plasma sources. *IEEE Trans. Plasma Sci.* **1998**, *26*, 1685–1694. [[CrossRef](#)]
2. Laroussi, M.; Akan, T. Arc-free atmospheric pressure cold plasma jets: A review. *Plasma Proc. Polym.* **2007**, *4*, 777–788. [[CrossRef](#)]
3. Chen, J.-Z.; Wang, C.; Hsu, C.-C.; Cheng, I.-C. Ultrafast synthesis of carbon-nanotube counter electrodes for dye-sensitized solar cells using an atmospheric-pressure plasma jet. *Carbon* **2016**, *98*, 34–40. [[CrossRef](#)]
4. Chou, C.-Y.; Chang, H.; Liu, H.-W.; Yang, Y.-J.; Hsu, C.-C.; Cheng, I.-C.; Chen, J.-Z. Atmospheric-pressure-plasma-jet processed nanoporous TiO₂ photoanodes and Pt counter-electrodes for dye-sensitized solar cells. *RSC Adv.* **2015**, *5*, 45662–45667. [[CrossRef](#)]
5. Wan, T.-H.; Chiu, Y.-F.; Chen, C.-W.; Hsu, C.-C.; Cheng, I.; Chen, J.-Z. Atmospheric-pressure plasma jet processed Pt-decorated reduced graphene oxides for counter-electrodes of dye-sensitized solar cells. *Coatings* **2016**, *6*, 44. [[CrossRef](#)]
6. Wu, T.J.; Chou, C.Y.; Hsu, C.M.; Hsu, C.C.; Chen, J.Z.; Cheng, I.C. Ultrafast synthesis of continuous Au thin films from chloroauric acid solution using an atmospheric pressure plasma jet. *RSC Adv.* **2015**, *5*, 99654–99657. [[CrossRef](#)]
7. Liu, L.; Ye, D.; Yu, Y.; Liu, L.; Wu, Y. Carbon-based flexible micro-supercapacitor fabrication via mask-free ambient micro-plasma-jet etching. *Carbon* **2017**, *111*, 121–127. [[CrossRef](#)]
8. Kuok, F.-H.; Kan, K.-Y.; Yu, I.-S.; Chen, C.-W.; Hsu, C.-C.; Cheng, I.-C. Application of atmospheric-pressure plasma jet processed carbon nanotubes to liquid and quasi-solid-state electrolyte supercapacitors. *Appl. Surf. Sci.* **2017**, *425*, 321–328. [[CrossRef](#)]
9. Yang, C.-H.; Kuok, F.-H.; Liao, C.-Y.; Wan, T.-H.; Chen, C.-W.; Hsu, C.-C.; Cheng, I.-C.; Chen, J.-Z. Flexible reduced graphene oxide supercapacitor fabricated using a nitrogen dc-pulse atmospheric-pressure plasma jet. *Mater. Res. Express* **2017**, *4*, 025504. [[CrossRef](#)]
10. Liu, H.W.; Liang, S.P.; Wu, T.J.; Chang, H.; Kao, P.K.; Hsu, C.C.; Chen, J.Z.; Chou, P.T.; Cheng, I.C. Rapid atmospheric pressure plasma jet processed reduced graphene oxide counter electrodes for dye-sensitized solar cells. *ACS Appl. Mater. Interfaces* **2014**, *6*, 15105–15112. [[CrossRef](#)] [[PubMed](#)]

11. Kuok, F.H.; Liao, C.Y.; Wan, T.H.; Yeh, P.W.; Cheng, I.C.; Chen, J.Z. Atmospheric pressure plasma jet processed reduced graphene oxides for supercapacitor application. *J. Alloys Compd.* **2017**, *692*, 558–562. [[CrossRef](#)]
12. Chen, S.L.; Wang, S.; Wang, Y.B.; Guo, B.H.; Li, G.Q.; Chang, Z.S.; Zhang, G.J. Surface modification of epoxy resin using He/CF₄ atmospheric pressure plasma jet for flashover withstanding characteristics improvement in vacuum. *Appl. Surf. Sci.* **2017**, *414*, 107–113. [[CrossRef](#)]
13. Munoz, J.; Bravo, J.A.; Calzada, M.D. Aluminum metal surface cleaning and activation by atmospheric-pressure remote plasma. *Appl. Surf. Sci.* **2017**, *407*, 72–81. [[CrossRef](#)]
14. Tsai, J.-H.; Cheng, I.-C.; Hsu, C.-C.; Chen, J.-Z. Dc-pulse atmospheric-pressure plasma jet and dielectric barrier discharge surface treatments on fluorine-doped tin oxide for perovskite solar cell application. *J. Phys. D: Appl. Phys.* **2017**, *51*, 025502. [[CrossRef](#)]
15. Bose, A.C.; Shimizu, Y.; Mariotti, D.; Sasaki, T.; Terashima, K.; Koshizaki, N. Flow rate effect on the structure and morphology of molybdenum oxide nanoparticles deposited by atmospheric-pressure microplasma processing. *Nanotechnology* **2006**, *17*, 5976–5982. [[CrossRef](#)]
16. Babayan, S.; Jeong, J.; Schütze, A.; Tu, V.; Moravej, M.; Selwyn, G.; Hicks, R. Deposition of silicon dioxide films with a non-equilibrium atmospheric-pressure plasma jet. *Plasma Sources Sci. Technol.* **2001**, *10*, 573. [[CrossRef](#)]
17. Patel, J.; Nemcova, L.; Maguire, P.; Graham, W.G.; Mariotti, D. Synthesis of surfactant-free electrostatically stabilized gold nanoparticles by plasma-induced liquid chemistry. *Nanotechnology* **2013**, *24*, 245604. [[CrossRef](#)] [[PubMed](#)]
18. Lee, C.-C.; Wan, T.-H.; Hsu, C.-C.; Cheng, I.-C.; Chen, J.-Z. Atmospheric-pressure plasma jet processed Pt/ZnO composites and its application as counter-electrodes for dye-sensitized solar cells. *Appl. Surf. Sci.* **2018**, *436*, 690–696. [[CrossRef](#)]
19. Malecki, S.; Gargul, K. Low-waste recycling of spent CuO-ZnO-Al₂O₃ catalysts. *Metals* **2018**, *8*, 177. [[CrossRef](#)]
20. Paiva, A.P. Recycling of palladium from spent catalysts using solvent extraction-some critical points. *Metals* **2017**, *7*, 505. [[CrossRef](#)]
21. Fujita, T.; Higuchi, K.; Yamamoto, Y.; Tokunaga, T.; Arai, S.; Abe, H. In-situ TEM study of a nanoporous Ni-Co catalyst used for the dry reforming of methane. *Metals* **2017**, *7*, 406. [[CrossRef](#)]
22. Joo, S.H.; Shin, D.J.; Oh, C.H.; Wang, J.P.; Park, J.T.; Shin, S.M. Application of Co and Mn for a Co-Mn-Br or Co-Mn-C₂H₃O₂ petroleum liquid catalyst from the cathode material of spent lithium ion batteries by a hydrometallurgical route. *Metals* **2017**, *7*, 439. [[CrossRef](#)]
23. Tai, M.C.; Gentle, A.; de Silva, K.S.B.; Arnold, M.D.; van der Lingen, E.; Cortie, M.B. Thermal stability of nanoporous raney gold catalyst. *Metals* **2015**, *5*, 1197–1211. [[CrossRef](#)]
24. Sabitu, S.T.; Goudy, A.J. Dehydrogenation kinetics and modeling studies of MgH₂ enhanced by transition metal oxide catalysts using constant pressure thermodynamic driving forces. *Metals* **2012**, *2*, 219–228. [[CrossRef](#)]
25. Song, H.; Hu, F.Y.; Peng, Y.; Li, K.Z.; Bai, S.P.; Li, J.H. Non-thermal plasma catalysis for chlorobenzene removal over CoMn/TiO₂ and CeMn/TiO₂: Synergistic effect of chemical catalysis and dielectric constant. *Chem. Eng. J.* **2018**, *347*, 447–454. [[CrossRef](#)]
26. O'regan, B.; Grätzel, M. A low-cost, high-efficiency solar cell based on dye-sensitized. *Nature* **1991**, *353*, 737–740. [[CrossRef](#)]
27. Lin, C.-Y.; Lin, J.-Y.; Wan, C.-C.; Wei, T.-C. High-performance and low platinum loading electrodeposited-Pt counter electrodes for dye-sensitized solar cells. *Electrochim. Acta* **2011**, *56*, 1941–1946. [[CrossRef](#)]
28. Bae, K.-H.; Park, E.; Dao, V.-D.; Choi, H.-S. PtZn nanoalloy counter electrodes as a new avenue for highly efficient dye-sensitized solar cells. *J. Alloys Compd.* **2017**, *702*, 449–457. [[CrossRef](#)]
29. Dao, V.D.; Nang, L.V.; Kim, E.T.; Lee, J.K.; Choi, H.S. Pt nanoparticles immobilized on CVD-grown graphene as a transparent counter electrode material for dye-sensitized solar cells. *ChemSusChem* **2013**, *6*, 1316–1319. [[CrossRef](#)] [[PubMed](#)]
30. Li, C.-T.; Chang, H.-Y.; Li, Y.-Y.; Huang, Y.-J.; Tsai, Y.-L.; Vittal, R.; Sheng, Y.-J.; Ho, K.-C. Electrocatalytic zinc composites as the efficient counter electrodes of dye-sensitized solar cells: Study on the electrochemical performances and density functional theory calculations. *ACS Appl. Mater. Interfaces* **2015**, *7*, 28254–28263. [[CrossRef](#)] [[PubMed](#)]

31. Wan, J.; Fang, G.; Yin, H.; Liu, X.; Liu, D.; Zhao, M.; Ke, W.; Tao, H.; Tang, Z. Pt–Ni alloy nanoparticles as superior counter electrodes for dye-sensitized solar cells: Experimental and theoretical understanding. *Adv. Mater.* **2014**, *26*, 8101–8106. [[CrossRef](#)] [[PubMed](#)]
32. Wang, H.; Wei, W.; Hu, Y.H. Efficient ZnO-based counter electrodes for dye-sensitized solar cells. *J. Mater. Chem. A* **2013**, *1*, 6622–6628. [[CrossRef](#)]
33. Yang, Q.; Duan, J.; Yang, P.; Tang, Q. Counter electrodes from platinum alloy nanotube arrays with zno nanorod templates for dye-sensitized solar cells. *Electrochim. Acta* **2016**, *190*, 648–654. [[CrossRef](#)]
34. Tang, Q.; Duan, J.; Duan, Y.; He, B.; Yu, L. Recent advances in alloy counter electrodes for dye-sensitized solar cells. A critical review. *Electrochim. Acta* **2015**, *178*, 886–899. [[CrossRef](#)]
35. Nechiyil, D.; Vinayan, B.P.; Ramaprabhu, S. Tri-iodide reduction activity of ultra-small size ptfе nanoparticles supported nitrogen-doped graphene as counter electrode for dye-sensitized solar cell. *J. Colloid Interface Sci.* **2017**, *488*, 309–316. [[CrossRef](#)] [[PubMed](#)]
36. Jin, I.-K.; Dao, V.-D.; Larina, L.L.; Choi, H.-S. Optimum engineering of a PtSn alloys/reduced graphene oxide nanohybrid for a highly efficient counter electrode in dye-sensitized solar cells. *J. Ind. Eng. Chem.* **2016**, *36*, 238–244. [[CrossRef](#)]
37. Zhu, Y.J.; Gao, C.J.; Han, Q.J.; Wang, Z.; Wang, Y.R.; Zheng, H.K.; Wu, M.X. Large-scale high-efficiency dye-sensitized solar cells based on a Pt/carbon spheres composite catalyst as a flexible counter electrode. *J. Catal.* **2017**, *346*, 62–69. [[CrossRef](#)]
38. Jiang, L.; Sun, G.; Sun, S.; Liu, J.; Tang, S.; Li, H.; Zhou, B.; Xin, Q. Structure and chemical composition of supported Pt–Sn electrocatalysts for ethanol oxidation. *Electrochim. Acta* **2005**, *50*, 5384–5389. [[CrossRef](#)]
39. Baranova, E.A.; Padilla, M.A.; Halevi, B.; Amir, T.; Artyushkova, K.; Atanassov, P. Electrooxidation of ethanol on PtSn nanoparticles in alkaline solution: Correlation between structure and catalytic properties. *Electrochim. Acta* **2012**, *80*, 377–382. [[CrossRef](#)]
40. Pang, H.; Lu, J.; Chen, J.; Huang, C.; Liu, B.; Zhang, X. Preparation of SnO₂-CNTs supported Pt catalysts and their electrocatalytic properties for ethanol oxidation. *Electrochim. Acta* **2009**, *54*, 2610–2615. [[CrossRef](#)]
41. Ordonez, L.C.; Roquero, P.; Sebastian, P.J.; Ramirez, J. Carbon-supported platinum-molybdenum electro-catalysts for methanol oxidation. *Catal. Today* **2005**, *107*, 46–52. [[CrossRef](#)]
42. Jiang, L.H.; Sun, G.Q.; Zhou, Z.H.; Xin, Q. Preparation and characterization of PtSn/C anode electrocatalysts for direct ethanol fuel cell. *Catal. Today* **2004**, *93*, 665–670. [[CrossRef](#)]
43. Jiang, W.; Pang, Y.J.; Gu, L.L.; Yao, Y.; Su, Q.; Ji, W.J.; Au, C.T. Structurally defined SnO₂ substrates, nanostructured Au/SnO₂ interfaces, and their distinctive behavior in benzene and methanol oxidation. *J. Catal.* **2017**, *349*, 183–196. [[CrossRef](#)]
44. Lee, B.; Sakamoto, Y.; Hirabayashi, D.; Suzuki, K.; Hibino, T. Direct oxidation of methane to methanol over proton conductor/metal mixed catalysts. *J. Catal.* **2010**, *271*, 195–200. [[CrossRef](#)]
45. Xie, J.H.; Falcone, D.D.; Davis, R.J. Restructuring of supported PtSn bimetallic catalysts during aqueous phase oxidation of 1,6-hexanediol. *J. Catal.* **2015**, *332*, 38–50. [[CrossRef](#)]
46. Mädler, L.; Roessler, A.; Pratsinis, S.E.; Sahm, T.; Gurlo, A.; Barsan, N.; Weimar, U. Direct formation of highly porous gas-sensing films by in situ thermophoretic deposition of flame-made Pt/SnO₂ nanoparticles. *Sens. Actuators B Chem.* **2006**, *114*, 283–295. [[CrossRef](#)]
47. Antolini, E. Formation of carbon-supported PtM alloys for low temperature fuel cells: A review. *Mater. Chem. Phys.* **2003**, *78*, 563–573. [[CrossRef](#)]
48. Khelashvili, G.; Behrens, S.; Hinsch, A.; Habicht, W.; Schild, D.; Eichhöfer, A.; Sastrawan, R.; Skupien, K.; Dinjus, E.; Bönnemann, H. Preparation and characterization of low platinum loaded Pt: SnO₂ electrocatalytic films for screen printed dye solar cell counter electrode. *Thin Solid Films* **2007**, *515*, 4074–4079. [[CrossRef](#)]
49. Sun, H.; Ullah, R.; Chong, S.; Ang, H.M.; Tade, M.O.; Wang, S. Room-light-induced indoor air purification using an efficient Pt/N-TiO₂ photocatalyst. *Appl. Catal. B Environ.* **2011**, *108*, 127–133. [[CrossRef](#)]
50. Ma, Y.; Wang, H.; Ji, S.; Linkov, V.; Wang, R. PtSn/C catalysts for ethanol oxidation: The effect of stabilizers on the morphology and particle distribution. *J. Power Sources* **2014**, *247*, 142–150. [[CrossRef](#)]
51. Xu, J.; Liu, X.; Chen, Y.; Zhou, Y.; Lu, T.; Tang, Y. Platinum–cobalt alloy networks for methanol oxidation electrocatalysis. *J. Mater. Chem.* **2012**, *22*, 23659–23667. [[CrossRef](#)]
52. Zhang, Y.; Han, T.; Zhu, L.; Fang, J.; Xu, J.; Xu, P.; Li, X.; Liu, C.-C. Pt₃₅Cu₆₅ nanoarchitecture: A highly durable and effective electrocatalyst towards methanol oxidation. *Nanotechnology* **2015**, *26*, 135706. [[CrossRef](#)] [[PubMed](#)]

53. Silva, J.; De Souza, R.F.; Romano, M.A.; D’Villa-Silva, M.; Calegari, M.L.; Hammer, P.; Neto, A.O.; Santos, M.C. PtSnIr/C anode electrocatalysts: Promoting effect in direct ethanol fuel cells. *J. Braz. Chem. Soc.* **2012**, *23*, 1146–1153. [[CrossRef](#)]
54. García-Rodríguez, S.; Somodi, F.; Borbáth, I.; Margitfalvi, J.L.; Peña, M.A.; Fierro, J.L.G.; Rojas, S. Controlled synthesis of Pt-Sn/C fuel cell catalysts with exclusive Sn–Pt interaction: Application in co and ethanol electrooxidation reactions. *Appl. Catal. B Environ.* **2009**, *91*, 83–91. [[CrossRef](#)]
55. De la Fuente, J.G.; Rojas, S.; Martínez-Huerta, M.; Terreros, P.; Pena, M.; Fierro, J. Functionalization of carbon support and its influence on the electrocatalytic behaviour of Pt/C in H₂ and Co electrooxidation. *Carbon* **2006**, *44*, 1919–1929. [[CrossRef](#)]
56. Vilella, I.; De Miguel, S.; Scelza, O. Hydrogenation of citral on Pt and PtSn supported on activated carbon felts (ACF). *Latin Am. Appl. Res.* **2005**, *35*, 51–57.
57. Vilella, I.M.; de Miguel, S.R.; de Lecea, C.S.-M.; Linares-Solano, Á.; Scelza, O.A. Catalytic performance in citral hydrogenation and characterization of PtSn catalysts supported on activated carbon felt and powder. *Appl. Catal. A Gen.* **2005**, *281*, 247–258. [[CrossRef](#)]
58. Crabb, E.M.; Marshall, R.; Thompsett, D. Carbon monoxide electro-oxidation properties of carbon-supported PtSn catalysts prepared using surface organometallic chemistry. *J. Electrochem. Soc.* **2000**, *147*, 4440–4447. [[CrossRef](#)]
59. Gong, F.; Wang, H.; Wang, Z.-S. Self-assembled monolayer of graphene/Pt as counter electrode for efficient dye-sensitized solar cell. *Phys. Chem. Chem. Phys.* **2011**, *13*, 17676–17682. [[CrossRef](#)] [[PubMed](#)]
60. Yue, G.; Wu, J.; Xiao, Y.; Lin, J.; Huang, M.; Lan, Z.; Fan, L. Functionalized graphene/poly (3, 4-ethylenedioxythiophene): Polystyrenesulfonate as counter electrode catalyst for dye-sensitized solar cells. *Energy* **2013**, *54*, 315–321. [[CrossRef](#)]
61. Yin, X.; Xue, Z.; Liu, B. Electrophoretic deposition of Pt nanoparticles on plastic substrates as counter electrode for flexible dye-sensitized solar cells. *J. Power Sources* **2011**, *196*, 2422–2426. [[CrossRef](#)]
62. Sigdel, S.; Dubey, A.; Elbohy, H.; Aboagye, A.; Galipeau, D.; Zhang, L.; Fong, H.; Qiao, Q. Dye-sensitized solar cells based on spray-coated carbon nanofiber/TiO₂ nanoparticle composite counter electrodes. *J. Mater. Chem. A* **2014**, *2*, 11448–11453. [[CrossRef](#)]
63. Wang, Q.; Moser, J.-E.; Grätzel, M. Electrochemical impedance spectroscopic analysis of dye-sensitized solar cells. *J. Phys. Chem. B* **2005**, *109*, 14945–14953. [[CrossRef](#)] [[PubMed](#)]
64. Agarwala, S.; Thummalakunta, L.; Cook, C.; Peh, C.; Wong, A.; Ke, L.; Ho, G. Co-existence of LiI and KI in filler-free, quasi-solid-state electrolyte for efficient and stable dye-sensitized solar cell. *J. Power Sources* **2011**, *196*, 1651–1656. [[CrossRef](#)]
65. Jeong, H.; Pak, Y.; Hwang, Y.; Song, H.; Lee, K.H.; Ko, H.C.; Jung, G.Y. Enhancing the charge transfer of the counter electrode in dye-sensitized solar cells using periodically aligned platinum nanocups. *Small* **2012**, *8*, 3757–3761. [[CrossRef](#)] [[PubMed](#)]
66. Park, K.-H.; Kim, S.J.; Gomes, R.; Bhaumik, A. High performance dye-sensitized solar cell by using porous polyaniline nanotubes as counter electrode. *Chem. Eng. J.* **2015**, *260*, 393–398. [[CrossRef](#)]
67. Yue, G.; Wu, J.; Xiao, Y.; Huang, M.; Lin, J.; Lin, J.-Y. High performance platinum-free counter electrode of molybdenum sulfide–carbon used in dye-sensitized solar cells. *J. Mater. Chem. A* **2013**, *1*, 1495–1501. [[CrossRef](#)]
68. Zheng, X.J.; Guo, J.H.; Shi, Y.T.; Xiong, F.Q.; Zhang, W.H.; Ma, T.L.; Li, C. Low-cost and high-performance CoMoS₄ and NiMoS₄ counter electrodes for dye-sensitized solar cells. *Chem. Commun.* **2013**, *49*, 9645–9647. [[CrossRef](#)] [[PubMed](#)]

